

Electrochemical Stability of $ZnMn_2O_4$: Understanding Zn-Ion Rechargeable Battery Capacity and Degradation

Oleg Rubel,* Thuy Nguyen Thanh Tran, Storm Gourley, Sriram Anand, Andrew Van Bommel, Brian D. Adams,* Douglas G. Ivey,* and Drew Higgins*



Cite This: *J. Phys. Chem. C* 2022, 126, 10957–10967



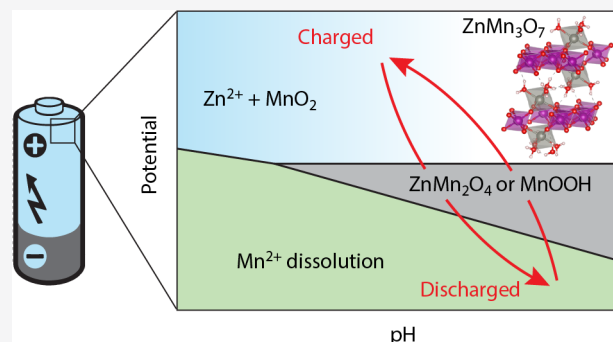
Read Online

ACCESS |

Metrics & More

Article Recommendations

ABSTRACT: We present a refined Mn–Zn–H₂O Pourbaix diagram with the emphasis on parameters relevant for the Zn/MnO₂ rechargeable cells. It maps out boundaries of electrochemical stability for MnO₂, ZnMn₂O₄, ZnMn₃O₇, and MnOOH. The diagram helps to rationalize experimental observation on processes and phases occurring during charge/discharge, including the position of charge/discharge redox peaks and capacity fade observed in rechargeable aqueous Zn-ion batteries for stationary storage. The proposed Pourbaix diagram is validated by observing the pH-dependent transformation of electrolytic manganese dioxide to hetaerolite and chalcophanite during discharge and charge, respectively. Our results can guide the selection of operating conditions (the potential range and pH) for existing aqueous Zn/MnO₂ rechargeable cells to maximise their longevity. In addition, the relation between electrochemical stability boundaries and operating conditions can be used as an additional design criterion in exploration of future cathode materials for aqueous rechargeable batteries.



INTRODUCTION

Eco-friendly rechargeable Zn-ion batteries with aqueous electrolyte have emerged as a cheaper and safer alternative to Li-ion batteries for certain applications such as grid scale energy storage.¹ In the first realization of an aqueous rechargeable Zn-ion battery, MnO₂ was used as the cathode (positive electrode) material.² Since then, polymorphs of MnO₂ remain a material of choice for fabrication of practical cells in spite of a variety of alternative positive electrode materials reported to date.¹ Reversible Zn²⁺ intercalation/deintercalation (discharging/charging) in the MnO₂ host framework and formation of ZnMn₂O₄ combined with H⁺ co-intercalation are recognized as the main energy storage mechanisms in Zn/MnO₂ cells.^{3–5}

Cycling performance of the Zn/MnO₂ cell is limited by capacity fade, especially at slower cycling rates⁶ that are necessary for grid-scale energy storage applications. This capacity fade is attributed to dissolution of the active cathode material into the electrolyte (formation of Mn^{2+(aq)})^{7–9} as well as the formation of irreversible phases at the cathode side, such as Mn(OH)₂, Mn₃O₄, or even ZnMn₂O₄.¹⁰ Current literature is ambiguous about the electrode potential where the dissolution takes place. For instance, Chao et al.¹¹ suggested that Mn²⁺ leaches at high voltages (greater than 1.7 V vs Zn^{0/Zn²⁺}). On the other hand, Li et al.⁶ attributed capacity fade to reactions that take place at lower voltages (less than 1.26 V vs

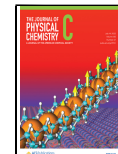
Zn^{0/Zn²⁺}). It seems that another solid phase ZnMn₃O_{7·nH₂O} (chalcophanite) is also involved in capacity fade.⁶ After the initial discharge process, the formation of chalcophanite was observed using X-ray diffraction, and the diffraction peaks associated with this phase became more intense as the cycle number increased, especially at slower cycle rates.⁶ Finally, Li et al.⁶ associated the formation of ZnMn₃O_{7·nH₂O} and Mn₃O₄ below 1.26 V vs Zn^{0/Zn²⁺} with capacity fade at slow cycling rates. Tran et al.¹² also reported ZnMn₃O_{7·3H₂O} in *ex situ* studies of Zn/EMD cells (EMD stands for electrolytic manganese dioxide¹¹) and linked the formation of chalcophanite with the electrochemical deposition of dissolved Mn²⁺ back on the cathode surface during charging at higher voltages (1.8 V vs Zn^{0/Zn²⁺}).

While battery operation is governed by non-equilibrium kinetic processes, understanding which phases of the Mn–Zn–H₂O system are stable within the range of parameters relevant for operation of rechargeable batteries will be important for explaining current stability limitations and designing electrode

Received: March 18, 2022

Revised: June 5, 2022

Published: June 30, 2022



structures that can provide extended operational lifetimes. In this sense, for aqueous batteries Pourbaix diagrams can be useful for displaying the equilibrium electrochemical stability of a metal–H₂O system. For example, Bischoff et al.¹³ created an overlay of Mn–H₂O and Zn–H₂O Pourbaix diagrams and measured *in situ* local changes in pH (3–5) during the battery cycle within the relevant range of the potential window 0.9–1.9 V vs Zn⁰/Zn²⁺. This diagram allows for several important conclusions: (i) MnO₂ and Mn₂O₃ are the only solid phases of the Mn–H₂O system that are stable in the range specified; (ii) at higher potentials (greater than 1.7 V vs Zn⁰/Zn²⁺) the only danger is electrolyte decomposition (via the O₂ evolution reaction) and not cathode dissolution; (iii) during discharge there is a problematic region (below ca. 1 V vs Zn⁰/Zn²⁺ at pH 5.5) where Mn²⁺(aq) is more stable than solid MnO₂. However, the diagram presented by Bischoff et al.¹³ does not consider stability boundaries of two important solids: hetaerolite ZnMn₂O₄ and chalcophanite ZnMn₃O₇·3H₂O.

Huang et al.¹⁴ proposed a ternary Mn–Zn–H₂O Pourbaix diagram, yet it does not have many details in the electrochemical potential region of interest for Zn-ion batteries. Qualitatively, the diagram shows the existence of ZnMn₂O₄ and Zn₂Mn₃O₈, but does not present clear boundaries for those phases. Also, ZnMn₃O₇·3H₂O does not appear on this diagram even though it was extensively discussed in the text of ref 14. It remains unclear what role these Zn-containing phases play in energy storage with respect to the operation of rechargeable Zn-ion batteries with aqueous electrolyte.

To elucidate the electrochemical stability of ZnMn₂O₄, we have provided detailed Mn–Zn–H₂O Pourbaix analysis focusing on the relevant range of parameters that are encountered in state of the art rechargeable Zn-ion batteries employing a Zn-sulfate electrolyte:¹³ namely, pH 4–6 and E_{Zn⁰/Zn²⁺} = 1.1–1.8 V. The new diagram outlines the electrochemical potential and pH regions of ZnMn₂O₄, ZnMn₃O₇·3 H₂O, and MnOOH stability. Conclusions drawn from the Pourbaix diagram are corroborated by experimental measurements of the cyclic performance of Zn/EMD cells at variable discharge potentials combined with *ex situ* studies of the cathode material, which provide critical fundamental insight to help understand the stability limitations of conventional electrode structures and guide improved material designs or operational parameters.

METHODS

Pourbaix Diagram. Even though construction of Pourbaix diagrams based on electronic structure calculations has become increasingly accurate,^{15–18} it is still not fully *ab initio* (mostly hindered by correlation effects of transition metals and finite-temperature thermodynamic properties). Here we build the Pourbaix diagram based on experimental data following the method established by Pourbaix¹⁹ and use a density functional theory (DFT) only when there are no experimental data. A key ingredient for construction of Pourbaix diagrams is standard chemical potentials μ° of species, listed in Table 1 at standard conditions per formula unit (f.u.).

In our calculations we assume concentrations of aqueous species at 2 M for Zn²⁺ and 0.1 M for Mn²⁺. These values are based upon typical concentrations of ZnSO₄ and MnSO₄ used in experimental Zn-ion battery research.^{7,9,13} The concentration of aqueous species is taken into account when computing their chemical potential (eV), e.g.,

Table 1. Chemical Potentials of Species Involved in Reactions^a

Species	μ° (eV/f.u.)	Ref.
Zn ²⁺ (aq)	-1.526	19
Mn ²⁺ (aq)	-2.359	19
MnO ₄ ⁻ (aq)	-4.657	19
H ₂ O(l)	-2.458	19
MnO ₂ (pyrolusite)	-4.83	20
MnOOH (manganite)	-5.81	21 (estimated from E [°] = 0.98 V at pH 0)
	-5.88	14 (Table S7 in Supporting Information)
ZnO	-3.292	22
ZnO hydr.	-3.336	19
α -Mn ₂ O ₃	-9.206	19
ZnMn ₂ O ₄ (hetaerolite)	-12.61	23
	-12.72	14 (Supporting Information)
ZnMn ₃ O ₇	-17.83 - $\delta\mu$	$\mu^\circ(\text{ZnO hydr.}) + 3\mu^\circ(\text{MnO}_2) - \delta\mu$
(chalcophanite) hydr.		

^aBold font highlights primary values used in calculations in the case of multiple values reported in the literature.

$$\mu(\text{Mn}^{2+}) = \mu^\circ(\text{Mn}^{2+}) + 0.0592 \log_{10}[\text{Mn}^{2+}] \quad (1)$$

where [Mn²⁺] is the aqueous concentration of Mn²⁺ ions. Sample calculations are presented in the Appendix. It should be noted that experiments in this paper were performed using an electrolyte with 1 M concentration of ZnSO₄ (see section Electrode Fabrication). This discrepancy has a minor effect on the calculated Pourbaix diagram and does not affect the main conclusions.

Electronic Structure Calculations. DFT^{24,25} calculations were performed using the Vienna *ab initio* simulation package²⁶ (VASP) and projector augmented-wave potentials.^{26–28} The following potentials were used: Mn_sv, Zn, O_h, H_h. A Perdew–Burke–Ernzerhof²⁹ (PBE) generalized gradient approximation (GGA) for the exchange-correlation functional was chosen in combination with the Grimme et al.³⁰ (D3) correction to capture long-range van der Waals interactions.

A full structural relaxation was conducted for all simulated compounds, which included relaxation of atomic positions (maximum Cartesian force component of 0.05 eV/Å) and stresses (1 kBar as the maximum component of the stress tensor). A cutoff energy of E_{cut} = 875 eV for the plane-wave expansion was used, which corresponds to the maximum value recommended in pseudopotential files further increased by 25% above (VASP tag PREC = High). The Brillouin zone was sampled using a Monkhorst and Pack³¹ shifted *k* mesh with a density of 20 divisions for every 1 Å⁻¹ linear dimension in reciprocal space.

Magnetism was included for structures with manganese and the O₂ molecule. In the O₂ molecule the ordering is ferromagnetic. We tested all possible permutations of antiferromagnetic arrangements in addition to the ferromagnetic ordering for structures with manganese and selected the lowest total energy.

Electrode Fabrication. EMD is a commonly utilized electrode material for Zn-ion batteries^{12,32,33} and was selected for the current study. EMD shows significant advantages for practical applications such as low synthesis cost and large-scale commercial availability due to the history of being used as a cathode material in commercial alkaline batteries.³⁴ Other

MnO_2 materials, such as $\alpha\text{-MnO}_2$ or $\beta\text{-MnO}_2$, could have been chosen, but the effect on the Pourbaix diagram should be minimal (see discussion in the [Results section](#)) and does not affect the key findings of this study.

EMD was obtained from Bormann Specialty Materials (formerly Tronox). All chemicals were used as received without further purification. A proprietary slurry cast method was used to prepare EMD electrodes.³⁵ The Zn-ion battery cells were made from a frame of acrylic sheets and thin Ti current collectors. The Zn metal electrode was positioned on top of the cell and separated from the underlying MnO_2 electrode by three layers of filter paper (separator) soaked with electrolyte. The contact area between the electrodes and the electrolyte was 4 cm².

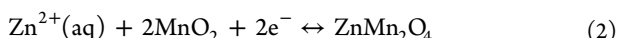
1 M zinc-sulfate aqueous electrolyte was prepared by adding ZnSO_4 to deionized water and stirring vigorously until completely dissolved. 1 M ZnSO_4 solutions with pH 2.5 and pH 4 were used as the electrolyte for the zinc-ion batteries. H_2SO_4 was added as needed to adjust the pH of the zinc sulfate electrolyte.

Electrochemical Testing and Characterization of EMD Electrodes. Electrochemical measurements were carried out with a Biologic SP-300 potentiostat. Batteries were first conditioned at a C-rate of $C/10$ and cycled at $C/5$. During the charging process, the batteries were held at 1.8 V for an additional 2 h or until the current density dropped to 8 $\mu\text{A mg}^{-1}$, whichever came first. After 5 cycles, EMD electrodes were extracted at fully discharged (0.9 V) and fully charged states (1.8 V, 2 h) for characterization.

The morphologies and compositions of the EMD electrodes were characterized using a scanning electron microscope (Tescan Vega3 SEM), coupled with an energy dispersive X-ray (EDX) spectrometer. X-ray diffraction (XRD) analysis was performed using a Rigaku Ultima IV diffractometer with monochromatic Cu K α X-radiation (wavelength equal to 1.54 Å) at a scan rate of 5 degrees min⁻¹. Transmission electron microscopy (TEM) and selected area electron diffraction (SAED) were performed using a JEOL JEM-ARM200CF TEM/STEM operating at an accelerating voltage of 200 kV.

RESULTS AND DISCUSSION

Electrochemical Stability of Hetaerolite and Zn^{2+} -Related Energy Storage. We began construction of the Mn–Zn–H₂O Pourbaix diagram by mapping out a region of stability for ZnMn_2O_4 (hetaerolite) as the only structure of MnO_2 with intercalated Zn for which thermodynamic properties are known. The charge and discharge of this structure with divalent Zn^{2+} ions is the key fundamental process occurring during rechargeable battery operation, which is governed by the reaction



Since there are no protons involved in this reaction, its equilibrium potential is $E_{\text{SHE}} = 0.72$ V (see [eq 12](#)) vs a standard hydrogen electrode (SHE), and it is independent of pH of the solution. The potential corresponds to the horizontal line (2) in [Figure 1](#), where the potential scale vs $\text{Zn}^0/\text{Zn}^{2+}$ is shown for convenience. The obtained equilibrium potential $E_{\text{Zn}^0/\text{Zn}^{2+}} = E_{\text{SHE}} - (-0.76)$ V ≈ 1.5 V for this reaction agrees well with the experimental average Zn^{2+} intercalation potential in MnO_2 .³⁶ Here -0.76 V (ref [37](#), p 536) is the standard reversible potential that corresponds to the half cell reaction $\text{Zn}(\text{s}) \leftrightarrow$

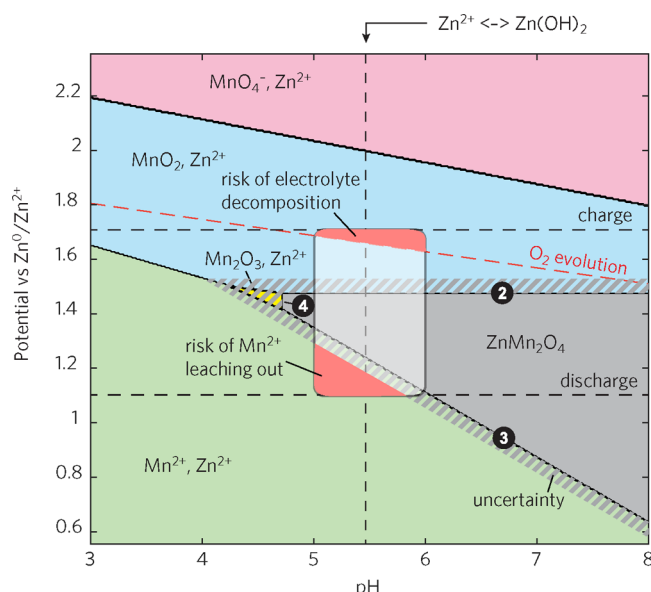
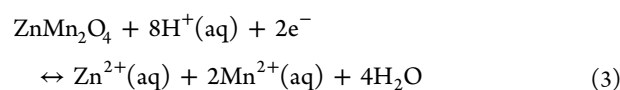


Figure 1. Mn–Zn–H₂O Pourbaix diagram with ZnMn_2O_4 phase boundaries. The battery operating window is shown as a wide bar. The hatched area reflects the uncertainty in the stability region of ZnMn_2O_4 due to the uncertainty in its chemical potential ([Table 1](#)). Phase boundaries marked with numbers are associated with the corresponding chemical reactions in the main text. The following concentrations of aqueous species are assumed: $[\text{Mn}^{2+}] = 0.1$ M, $[\text{Zn}^{2+}] = 2$ M, and $[\text{MnO}_4^-] = 0.1$ M.

$\text{Zn}^{2+}(\text{aq}) + 2\text{e}^-$. The calculated value of the equilibrium potential for [reaction 2](#) has a small uncertainty (ca. 0.05 V; see hatched region in [Figure 1](#)), which comes from two slightly different values of $\mu^\circ(\text{ZnMn}_2\text{O}_4)$ in [Table 1](#). The formation of hetaerolite is experimentally confirmed in Zn/EMD cells after discharge at 1.35 V vs $\text{Zn}^0/\text{Zn}^{2+}$,¹² which supports our diagram ([Figure 1](#)).

Here, we use pyrolusite ($\beta\text{-MnO}_2$) as a reference for $\mu^\circ(\text{MnO}_2)$ since it is the most stable natural form of MnO_2 .³⁸ Other MnO_2 polymorphs are used in batteries, e.g., $\alpha\text{-MnO}_2$, as well as ϵ -, R-, and $\gamma\text{-MnO}_2$ as main constituents of EMD. The question is whether the structure of MnO_2 makes a significant difference to the Pourbaix diagram. We are not aware of any experimentally measured energy differences between the β phase and other polymorphs, but any differences can be inferred from DFT calculations. Our results suggest that $\beta\text{-MnO}_2$ has the lowest total energy followed by R- and $\gamma\text{-MnO}_2$ (both have an additional 0.01 eV/f.u. above $\beta\text{-MnO}_2$) and $\alpha\text{-MnO}_2$ (additional 0.05 eV/f.u.). Kitchaev et al.³⁹ came to a similar conclusion (ca. 0.05, 0.04, and 0.07 eV/f.u. for R, γ , and α phases) with a more chemically accurate metha-GGA exchange correlation functional. If $\alpha\text{-MnO}_2$ is used instead, the equilibrium potential for [reaction 2](#) would increase by 0.05 V, which is not critical for the purpose of our discussion and would fall within the error margins of experimental formation energies (see hatched region in [Figure 1](#)).

Now we turn to dissolution of the cathode material. It is expressed by the following reaction:



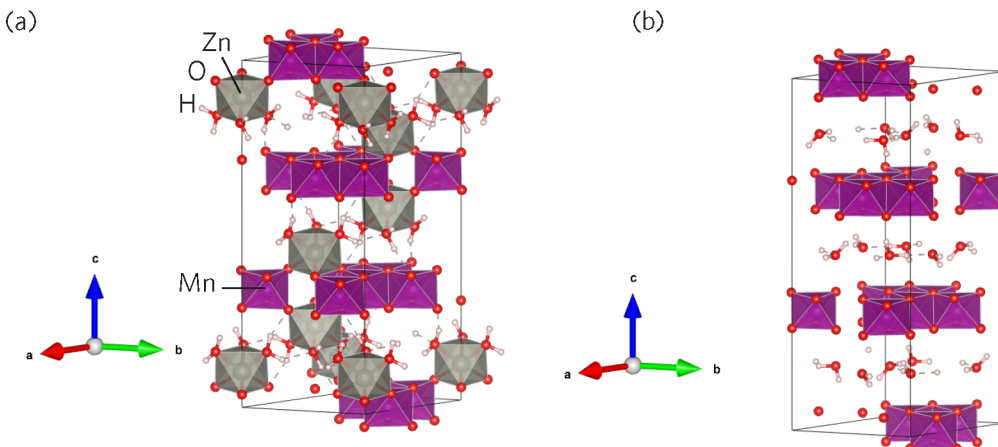
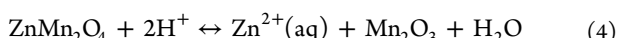


Figure 2. (a) Chalcophanite ZnMn₃O₇·3H₂O and (b) chalcophanite with deintercalated zinc Mn₃O₇·3H₂O.

The equilibrium potential for reaction 3 is $E_{\text{SHE}} = 1.78 \text{ V} - \text{pH} \times 0.237 \text{ V}$ (see eq 13), which is a function of pH as the reaction involves both water and protons. The dissolution boundary is marked as (3) in Figure 1 with the uncertainty as per the discussion above. Once we put this boundary in the context of the pH and potential range for Zn/MnO₂ battery operation (represented by a rectangle in Figure 1), we immediately recognize that the lower boundary of ZnMn₂O₄ electrochemical stability is close to the lower boundary of the discharge potential. This result is in line with Li et al.⁶ who attributed the capacity fade to a dissolution of the active cathode material into the electrolyte that takes place at lower voltages (less than 1.26 V vs Zn⁰/Zn²⁺). Tran et al.¹² reached a similar conclusion after experimental studies involving detection of soluble Mn²⁺ species formed during discharge, namely that Mn²⁺ is formed/dissolved at lower voltages (below ~1.1 V vs Zn⁰/Zn²⁺).

We can also see from the Pourbaix diagram in Figure 1 that a more acidic electrolyte (i.e., lower pH) favors cathode dissolution (pH < 5). At the same time, pH is buffered by the formation of Zn(OH)₂ (pH > 5.5). This leaves us with a narrow pH range of 5 < pH < 5.5 and a limited lowest discharge potential of $E_{\text{Zn}^0/\text{Zn}^{2+}}^{\text{min}} = 1.2 \text{ V}$ to avoid cathode corrosion.

To complete the map of ZnMn₂O₄ electrochemical stability, we also consider its transformation into Mn₂O₃



Here, the transition occurs at a fixed pH = 4.75 (line (4) in Figure 1) since the reaction does not involve electrons (see eq 14). This pH boundary value is extremely sensitive to chemical potentials of species involved in the reaction. The Mn₂O₃ region can even vanish (see hatched zone in Figure 1) with 0.1 eV uncertainty in $\mu^\circ(\text{ZnMn}_2\text{O}_4)$. This marks the pH boundary below which ZnMn₂O₄ is unstable, and thus, energy storage due to Zn²⁺ intercalation is not possible.

Chalcophanite. Chalcophanite (ZnMn₃O₇·3H₂O) is a byproduct phase formed in the cathode material of rechargeable aqueous Zn/MnO₂ batteries upon cycling (see section Introduction). To understand the role of ZnMn₃O₇·3H₂O in energy storage, we begin with a review of its crystal structure, as shown in Figure 2a. The stoichiometry can be viewed as a Mn_{0.86}O₂ manganese-deficient layered structure where two Zn atoms electronically compensate for each Mn vacancy. At first glance, we can expect the chalcophanite phase to participate in the energy storage similar to ZnMn₂O₄ where Zn²⁺ can be deintercalated by an applied potential. The question that comes to mind is regarding the magnitude of the potential. If the thermodynamic properties of ZnMn₃O₇·3H₂O were experimentally determined, we would follow the same approach used in the analysis of reaction 2. However, in the absence of experimental data we can only rely on DFT calculations.

Aydinol et al.⁴⁰ proposed a method for calculation of an average Li intercalation voltage \bar{E} in transition metal oxides based on DFT total energies H . The original expression modified for the case of ZnMn₃O₇·3H₂O is

$$\bar{E}_{\text{Zn}^0/\text{Zn}^{2+}} = \frac{H(\text{Zn}_{x_1}\text{Mn}_3\text{O}_7\cdot3\text{H}_2\text{O}) + (x_2 - x_1)H(\text{Zn}) - H(\text{Zn}_{x_2}\text{Mn}_3\text{O}_7\cdot3\text{H}_2\text{O})}{2e(x_2 - x_1)} \quad (5)$$

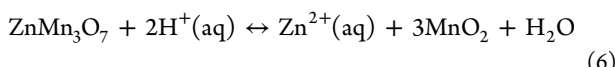
where $H(\text{Zn})$ is the DFT total energy of bulk Zn, e is the magnitude of the electron charge, and x_2 and x_1 are the effective number of Zn atoms in the structure before and after deintercalation ($x_1 < x_2$). The factor of two in the denominator reflects the ionic charge of Zn²⁺. Our structural model of ZnMn₃O₇·3H₂O ($x_2 = 1$) is based on experimental data reported by Post and Appleman⁴¹ (space group 148, $R\bar{3}$ hexagonal axes) with lattice parameters $a = b = 7.53 - 7.54 \text{ \AA}$ and $c = 20.79 - 20.82 \text{ \AA}$. DFT lattice parameters $a = b = 7.54 \text{ \AA}$ and $c = 20.51 \text{ \AA}$ were obtained after full structural relaxation. The structure of Mn₃O₇·3H₂O ($x_1 = 0$) with deintercalated Zn

(Figure 2b) was obtained by removing Zn followed by full structural relaxation. The total energies of these two structures as well as the bulk Zn were used to calculate the intercalation potential using eq 5.

The DFT-predicted Zn intercalation potential in ZnMn₃O₇·3H₂O is $\bar{E}_{\text{Zn}^0/\text{Zn}^{2+}} = 2.6 \text{ V}$ vs Zn⁰/Zn²⁺. This is a very large value compared to 1.5 V for ZnMn₂O₄. It should be noted that a DFT with PBE exchange-correlation functional always underestimates redox potentials relative to experiments due to its failure to properly capture correlation effects on the transition metal ion.⁴² Such a large Zn intercalation potential in

$\text{Zn}_{1/0}\text{Mn}_3\text{O}_7 \cdot 3\text{H}_2\text{O}$ can be attributed to the $\text{Mn}^{4+/5+}$ redox reaction instead of $\text{Mn}^{3+/4+}$ as in the case of $\text{Zn}_{1/0}\text{Mn}_2\text{O}_4$.

To add $\text{ZnMn}_3\text{O}_7 \cdot 3\text{H}_2\text{O}$ to the Pourbaix diagram, we need to identify its boundaries of stability. This task is complicated by the lack of its experimental chemical potential, and DFT calculations are still too inaccurate for this purpose. Thus, we assume $\mu^\circ(\text{ZnMn}_3\text{O}_7 \text{hydr.}) = \mu^\circ(\text{ZnO hydr.}) + 3\mu^\circ(\text{MnO}_2) - \delta\mu$, where $\delta\mu$ is a stability margin which will be kept as a variable. First, we investigate ZnMn_3O_7 decomposition with MnO_2 as one of the products



This reaction has no charge transfer and, thus, cannot be used for energy storage. The equilibrium boundary is at $\text{pH} = 5.32 - 0.118^{-1}\delta\mu$ ($\delta\mu$ should be in eV). Figure 3 presents the

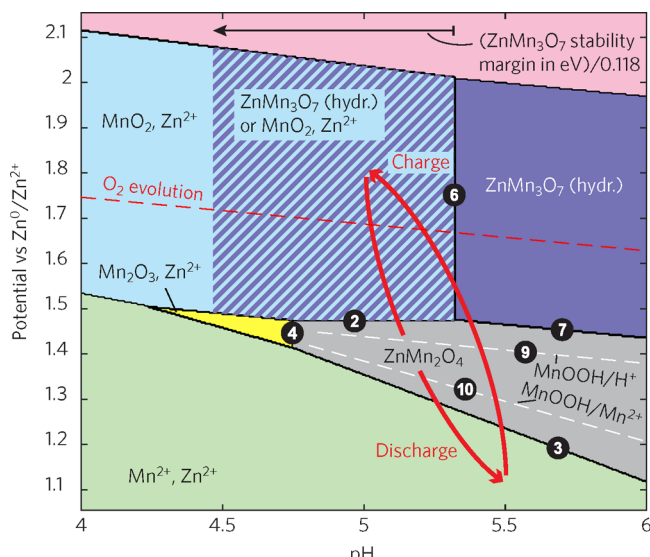
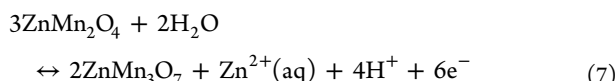


Figure 3. Mn–Zn–H₂O Pourbaix diagram with boundaries for ZnMn_2O_4 , ZnMn_3O_7 (hydr.), and MnOOH phases. The hatched region represent an uncertainty in ZnMn_3O_7 (hydr.) stability margin $\delta\mu = 0\text{--}0.1 \text{ eV/f.u.}$ A typical charge–discharge cycle of a Zn/MnO₂ cell is shown schematically. Phase boundaries marked with numbers are associated with the corresponding chemical reactions in the main text. The $\text{Zn}(\text{OH})_2$ stability boundary at pH 5.45 is not shown. The following concentrations of aqueous species are assumed: $[\text{Mn}^{2+}] = 0.1 \text{ M}$, $[\text{Zn}^{2+}] = 2 \text{ M}$, and $[\text{MnO}_4^-] = 0.1 \text{ M}$.

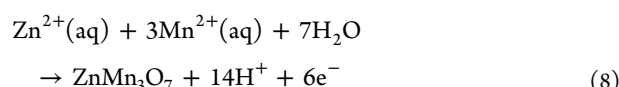
Pourbaix diagram with chalcophanite. The equilibrium boundary for this reaction, line (6), is included with the uncertainty region that reflects $\delta\mu = 0\text{--}0.1 \text{ eV}$. We believe that this is a correct order of magnitude for $\delta\mu$, as we did not observe chalcophanite experimentally at low pH values (see section Experimental Validation).

To map a boundary between chalcophanite and ZnMn_2O_4 we investigated the following reaction



that yields $E_{\text{SHE}} = 0.93 - \delta\mu/3\text{e} - 0.0395 \text{ pH}$ (line (7) in Figure 3). Here $\delta\mu$ has a marginal influence on the result. At pH 5.5 the boundary will be at 0.71 V vs SHE or 1.47 V vs $\text{Zn}^0/\text{Zn}^{2+}$, which barely affects the ZnMn_2O_4 stability range.

It is now possible to rationalize experimental observations related to chalcophanite in Zn/MnO₂ cells and its relation to capacity fading. The region of $\text{ZnMn}_3\text{O}_7 \cdot 3\text{H}_2\text{O}$ electrochemical stability on the Pourbaix diagram is in the location that was roughly outlined by Huang et al.¹⁴ for $\text{Zn}_2\text{Mn}_3\text{O}_8$. Tran et al.¹² also observed formation of chalcophanite after charging of Zn/EMD cells and maintaining the potential at 1.8 V vs $\text{Zn}^0/\text{Zn}^{2+}$ (hatched region in Figure 3) for 2 h. Most likely, reaction 6 is kinetically too slow and, instead, chalcophanite is deposited from dissolved aqueous species during battery charging¹² (hatched region in Figure 3).



Here the presence of $\text{Mn}^{2+}(\text{aq})$ in the electrolyte comes from the cathode material previously leached out during discharge, which explains the connection between chalcophanite formation and a deep discharge potential established by Li et al.⁶ Thus, chalcophanite acts as a scavenger in consuming dissolved $\text{Mn}^{2+}(\text{aq})$ species preventing them from depositing back as MnO_2 .

Here, we have not conducted calculations on the $\text{Zn}_2\text{Mn}_3\text{O}_8$ compound since we do not have enough knowledge about its structure, thermodynamics, and experimental evidence for its importance in battery cycling performance. Also, we have not discussed zinc hydroxide sulfate $\text{Zn}_4(\text{OH})_6(\text{SO}_4)\cdot x\text{H}_2\text{O}$; the relevant Pourbaix diagram of Zn–S–H₂O has been reported elsewhere.¹²

Complementary Energy Storage Mechanisms. It is widely discussed in the literature^{5,6,43,44} that the proton exchange reaction



has a significant contribution to energy storage in Zn/MnO₂ aqueous cells. Interestingly, MnOOH was not included in the original Mn–H₂O Pourbaix diagram,¹⁹ and its chemical potential was omitted. Bratsch²¹ reported that $E^\circ = 0.98 \text{ V}$ for this reaction with $\beta\text{-MnO}_2$ at pH = 0, which translates into $\mu^\circ(\text{MnOOH}) = -5.81 \text{ eV/f.u.}$ (There is an alternative value of $\mu^\circ(\text{MnOOH})$ listed in Table 1 that indicates the amount of scatter in the experimental data.)

According to eq 17 the corresponding H⁺ deintercalation potential in reaction 9 is $E_{\text{SHE}} = 0.98 - 0.0592 \text{ pH}$ (in V), which amounts to $E_{\text{Zn}^0/\text{Zn}^{2+}} = 1.41 \text{ V}$ at pH 5.5. This potential is very close to $E_{\text{Zn}^0/\text{Zn}^{2+}} \approx 1.5 \text{ V}$ for the Zn^{2+} deintercalation reaction, as shown in Figure 3 by lines (2) and (9). Magar et al.⁴⁵ arrived at the same result via DFT calculations, namely suggesting that proton insertion is only 0.1 eV less favorable than Zn^{2+} intercalation per MnO_2 formula unit. Since both energy mechanisms (Zn^{2+} and H⁺ deintercalation) require nearly the same voltage, we can conclude that both can coexist and contribute to energy storage in the Zn/MnO₂ aqueous cell. Cyclic voltammetry⁵ of Zn/MnO₂ cells also revealed two redox peaks upon both charge and discharge; the peaks were spaced 0.1–0.2 V apart (the same as our calculated equilibrium potentials for reactions 2 and 9 in Figure 3) and are attributed to two redox reactions that involve $\text{Zn}^{2+}/\text{H}^+$ intercalation in MnO_2 . It should be noted that the potential corresponding to reduction and oxidation peaks is sensitive ($\pm 0.1 \text{ V}$) to the crystal structure (polymorph) of MnO_2 , presence of defects, particle size, and morphology.^{7,46–52} This implies that

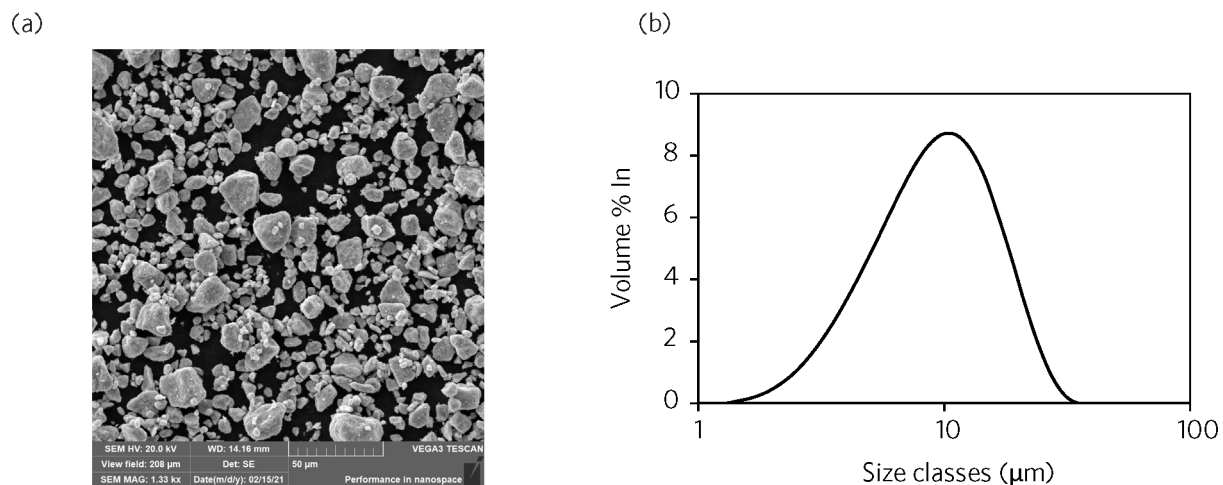


Figure 4. EMD particles: (a) SEM secondary electron (SE) image, (b) particle size distribution.

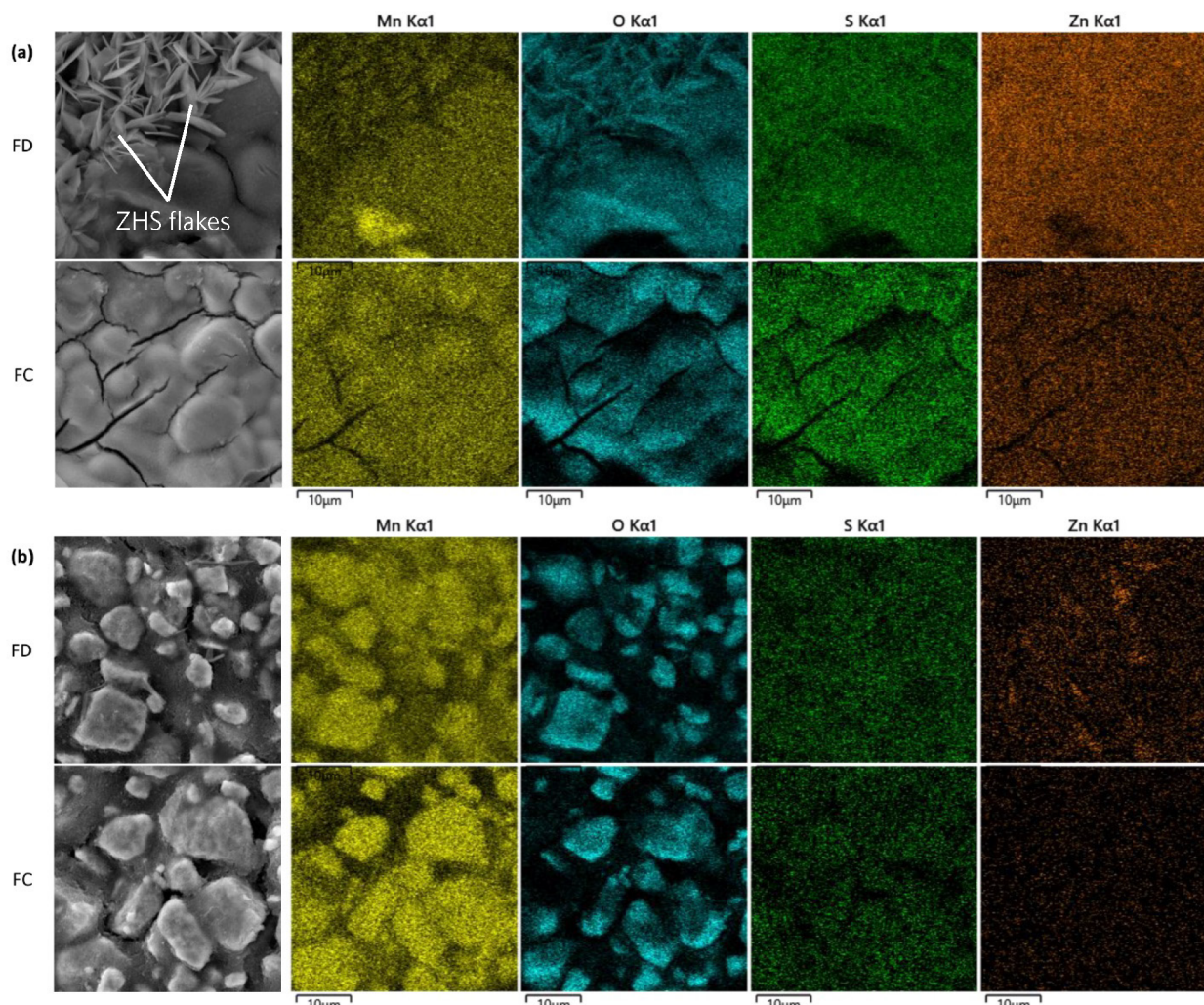


Figure 5. SEM SE images and corresponding EDX maps of EMD electrodes after 5 cycles in electrolytes with different pH values: (a) pH 4 and (b) pH 2.5. Fully discharged and fully charged states are denoted as FD and FC, respectively.

conclusions drawn from the Pourbaix diagram are robust with respect to those extrinsic factors.

MnOOH can also be further reduced to Mn²⁺(aq)



which takes place at $E_{\text{SHE}} = 1.52 - 0.178 \text{ pH}$ (in V) as shown in Figure 3, line (10). At pH 5.5, this amounts to an equilibrium potential of $E_{\text{Zn}^0/\text{Zn}^{2+}} = 1.31 \text{ V}$ slightly above that for the ZnMn_2O_4 dissolution/reduction reaction (see line (3) in Figure 3). This suggests that MnOOH is more susceptible to

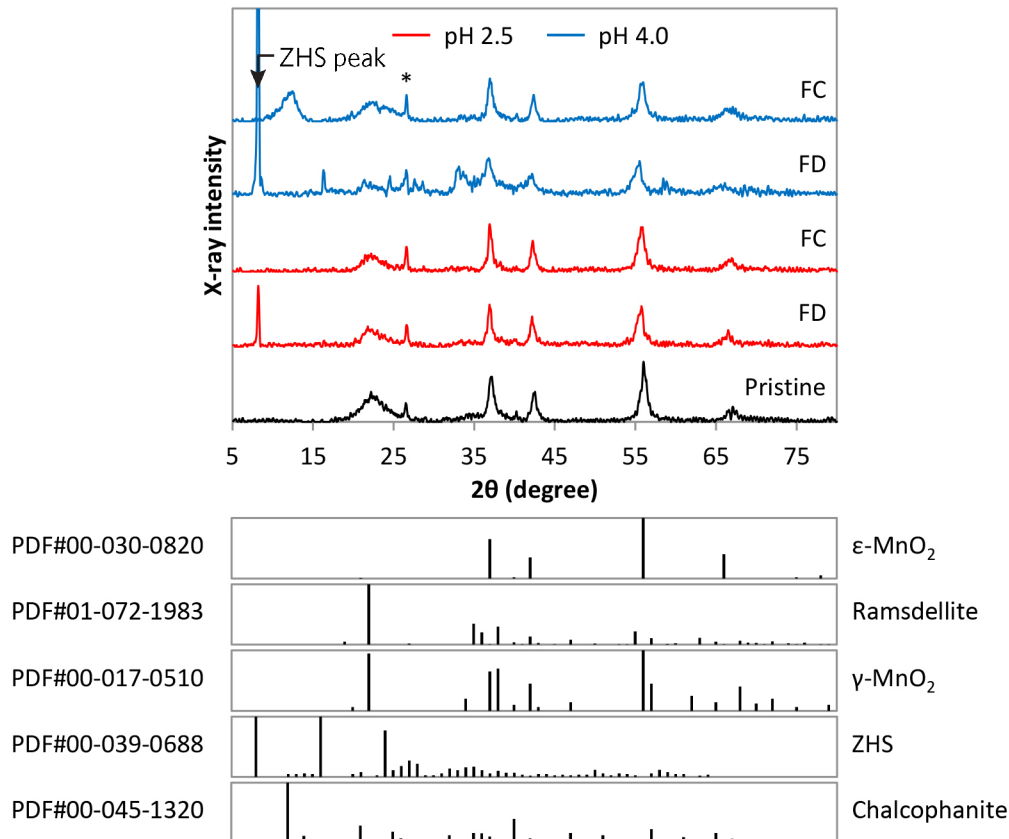
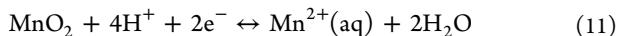


Figure 6. XRD patterns of EMD electrodes after 5 cycles during GCD tests in electrolytes with different pH values. Reference PDF cards for ϵ -MnO₂, ramsdellite, γ -MnO₂, ZHS, and chalcophanite are included at the bottom of the XRD patterns. Fully discharged and fully charged states are denoted as FD and FC, respectively. The asterisk indicates a graphite peak from the current collector.

dissolution/reduction than ZnMn₂O₄ during discharge. Interestingly, 1.31 V is remarkably close to 1.26 V vs Zn⁰/Zn²⁺ which is marked as a boundary for capacity fade reactions by Li et al.⁶

The cathode dissolution process (if reversible) can also participate in the energy storage via the following reaction



This reaction involves 2e⁻, while the conventional Zn intercalation **reaction 2** or the proton intercalation **reaction 9** involves only 1e⁻ per MnO₂ formula unit. Thus, the MnO₂ cathode dissolution results in a theoretical specific capacity of nearly 600 mA h g⁻¹. This is, however, quite an unrealistic figure assuming that the entire cathode dissolves in the electrolyte. Lee et al.⁸ presented experimental evidence for reversible dissolution of 1/3 of the α -MnO₂ cathode material during the charge–discharge cycle. According to this scenario, half of the energy storage capacity would come from Zn intercalation, and the other half would be contributed by cathode dissolution. Moon et al.⁵³ support this argument by finding *ex situ* a substantial amount of α -MnO₂ remaining unreacted even after full discharge even though the cell delivered ca. 90% of its theoretical specific capacity for Zn²⁺ or H⁺ intercalation. References 12 and 53 also provide experimental evidence for electrochemical co-deposition of chalcophanite from Mn²⁺(aq) and Zn²⁺(aq) species at the full charge state and its subsequent dissolution during discharge, which agrees with the Pourbaix diagram in Figure 3.

Experimental Validation. To validate the Zn–Mn–H₂O Pourbaix diagram in Figure 3, we constructed a set of experiments that involve *ex situ* characterization of the electrolytic MnO₂ cathode material after cycling. Different regions of the Pourbaix diagram were sampled by changing the acidity of the electrolyte (pH 2.5 and 4). These pH values reflect the “as prepared” electrolyte. During battery operation, the pH of the electrolyte evolves as a result of an increase in OH⁻ concentration during discharge followed by zinc hydroxide sulfate (ZHS) precipitation that buffers the pH to ~5.5.^{7,13,54} When the initial pH of the electrolyte was 4, ZHS started to appear at potentials below 1.35 V but before 1.18 V. For the electrolyte with an initial pH of 2.5, ZHS formation was suppressed and did not occur until after a potential of 1.18 V was reached.

Figure 4 shows EMD particles and their size distribution prior to electrode fabrication. There is a fairly wide distribution of particle size with a mean size of ca. 10 μm . Morphological changes of EMD electrodes after 5 cycles in electrolytes with different pH values are shown in Figure 5. For pH 4 (Figure 5a), during discharge, the electrode surface is covered with ZHS flakes and a new layer of Zn–Mn oxide, consisting of hetaerolite and Zn-intercalated Mn oxide. During charge, ZHS disappears while the new Zn–Mn-oxide layer remains. This new layer has a characteristic “desert crack pattern” without distinct particles; its morphology is very different from the original EMD electrode (see ref 12, Figure 6a therein). This suggests that this Zn–Mn-oxide layer was electrochemically deposited during cycling. More detailed SEM characterization

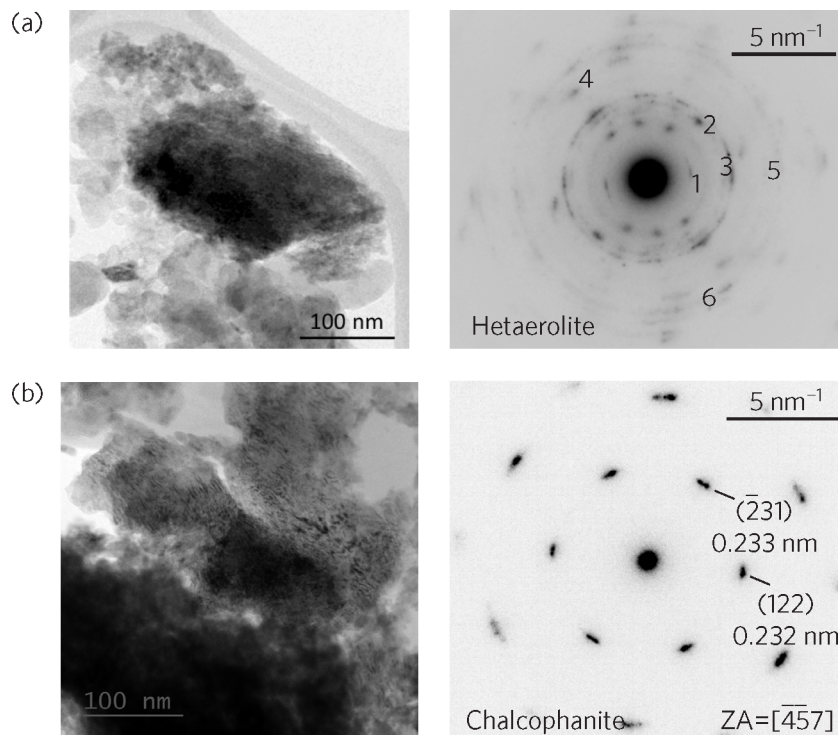


Figure 7. TEM bright field images and SAED patterns from the EMD electrodes at different stages during cycling at pH 4. (a) Electrode discharged at 1.35 V during the 1st cycle and (b) fully charged electrode held for 2 h at 1.8 V during the 50th cycle. The labels 1–6 on the SAED pattern for hetaerolite correspond to the d-spacings, in order, in Table 2.

of the EMD surface morphology before and after cycling including various charge and discharge depths is presented in ref 12.

For pH 2.5 (Figure 5b), the morphology of the EMD electrode surface is retained with little or no change. During discharge, a small amount of ZHS forms and its formation is reversible during charge. In general, all EDX maps show that the S signal overlaps with Zn; however, Zn has covered more of the electrode surface after cycling for the pH 4 solution than the pH 2.5 solution.

Pristine EMD has been characterized in ref 12. Briefly, the EMD powder is composed of about 53% ϵ -MnO₂, 34% ramsdellite, and 13% γ -MnO₂, determined through Rietveld refinement. XRD results of EMD electrodes after 5 cycles are shown in Figure 6. For both discharged electrodes (pH 4.0 and 2.5), a new peak appears at $\sim 8.1^\circ$ and corresponds to the formation of ZHS. The ZHS peak is significantly more intense for the pH 4.0 sample compared with the pH 2.5 sample, which indicates that more ZHS forms at the higher pH and corroborates the SEM results. During charge, the ZHS peaks disappear.

During discharge of the electrodes, the major peak ((102) plane) for ϵ -MnO₂ at 56° shifts to a lower angle of 55.8° and 55.5° at pH 2.5 and 4, respectively. All other major ϵ -MnO₂ peaks ((100), (101) and (110), originally at 37.1° , 42.5° and 67.0° , respectively) also shift to lower angles during discharge. The (102) peak shifts back to 55.9° after charging, meaning that the structure of ϵ -MnO₂ can expand and collapse almost reversibly to accommodate Zn²⁺ ions. In addition, for the charged electrode cycled in the electrolyte with a pH of 4, a new peak appears at 12.7° which matches the major peak for chalcophanite. This correlates well with the SEM images and EDX mapping of the Mn–Zn oxide layer that builds up on the

EMD electrode surface during cycling in the electrolyte with pH 4. This result also matches the Pourbaix diagram (Figure 3) with the pH buffering to 5.5 and a charge potential of 1.8 V vs Zn⁰/Zn²⁺. Chalcophanite is not observed for the electrolyte with pH 2.5, which is also expected from the Pourbaix diagram. The XRD results were not able to confirm the formation of hetaerolite (main peak is (211) at $\sim 36.5^\circ$) during discharge likely due to significant interference from both MnO₂ and ZHS peaks. However, the presence of hetaerolite was confirmed by electron diffraction in the TEM (Figure 7a).

According to Chamoun et al.,⁷ hetaerolite should not form if the EMD electrode is cycled in a more acidic electrolyte. Thus, only electrodes discharged at 1.35 V during the 1st cycle and fully charged at 1.8 V for 2 h during the 50th cycle in pH 4 are shown in Figure 7, including examples of SAED patterns from the particles shown. It should be noted that when Zn/MnO₂ batteries discharge, the pH of the electrolyte in the vicinity of the EMD electrodes should increase significantly. The SAED patterns in Figure 7a and b were indexed to hetaerolite (ZnMn₂O₄) (Table 2) and chalcophanite (ZnMn₃O₇), respectively. These results agree with the Pourbaix diagram in Figure 3.

CONCLUSIONS

We have presented a refined Mn–Zn–H₂O Pourbaix diagram with emphasis on the battery-relevant range of parameters (pH 4–6, $E_{\text{Zn}^0/\text{Zn}^{2+}} = 1.1$ –1.8 V). The diagram maps out boundaries of electrochemical stability for MnO₂, ZnMn₂O₄, ZnMn₃O₇, and MnOOH. The diagram helps to rationalize experimental observation of processes and phases occurring during the charge/discharge of Zn/MnO₂ aqueous cells. The average charge potential of 1.5 V vs Zn⁰/Zn²⁺ and the mid-potential value of the redox couple peaks (~ 1.4 V vs Zn⁰/Zn²⁺)

Table 2. Indexed d-Spacings for the SAED Pattern in Figure 7a and d-Spacings from the PDF Card for Hetaerolite (PDF#01-077-0407)

d-spacing (Å)	Hetaerolite	(hkl)
4.84	4.86	(101)
2.72	2.71	(103)
2.47	2.46	(211)
1.81	1.80	(204)
1.57	1.56	(321)
1.54	1.52	(224)

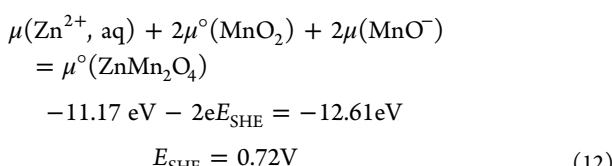
measured during cyclic voltammetry agree with the boundaries between ZnMn_2O_4 and MnO_2 for Zn^{2+} intercalation ($E_{\text{Zn}^0/\text{Zn}^{2+}} = 1.5$ V) or the boundary between MnOOH and MnO_2 for H^+ intercalation ($E_{\text{Zn}^0/\text{Zn}^{2+}} = 1.4$ V at pH 5.5). The experimentally observed capacity fade attributed to dissolution of ZnMn_2O_4 , MnOOH , or MnO_2 at low discharge potentials (below 1.1–1.2 V vs $\text{Zn}^0/\text{Zn}^{2+}$) agrees with the boundaries between these phases and aqueous Mn^{2+} ($E_{\text{Zn}^0/\text{Zn}^{2+}} \approx 1.2$ V at pH 5.5). At the same time, dissolution of the cathode material MnO_2 can make a sizable contribution to the specific capacity of the battery (up to 50%). The precipitation of chalcophanite ZnMn_3O_7 in a cathode material charged at 1.8 V correlates with its predicted range of stability above $E_{\text{Zn}^0/\text{Zn}^{2+}} \approx 1.5$ V at pH 5.5. Chalcophanite (formed at high voltages during charge) participates in capacity fade by consuming dissolved Mn^{2+} species and preventing their return back to MnO_2 . Unlike ZnMn_2O_4 , it is not feasible to deintercalate Zn^{2+} from ZnMn_3O_7 .

The impact of electrolyte pH has been investigated experimentally for aqueous zinc-ion MnO_2 batteries. For an electrolyte with pH 4, a fraction of pristine electrolytic manganese dioxide transforms to hetaerolite and chalcophanite during discharge and charge, respectively. The transformation does not occur when the pH of electrolyte is adjusted to 2.5, which validates the proposed Mn–Zn– H_2O Pourbaix diagram.

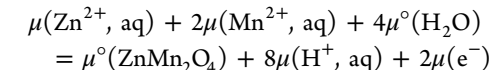
Making progress in understanding the reaction mechanisms responsible for capacity fade can provide insight to future researchers working on performance improvements to MnO_2 type cathodes. In addition, the electrochemical stability should be used as an additional design criterion in exploration of future cathode materials for aqueous rechargeable batteries.

APPENDIX: THERMODYNAMIC CALCULATIONS OF EQUILIBRIUM POTENTIALS

Here we show a detailed workflow to illustrate calculations of the equilibrium potential for the electrochemical reaction using thermodynamic data from Table 1 and assuming concentrations of aqueous species at 2 M for Zn^{2+} and 0.1 M for Mn^{2+} . Results are shown for the reaction 2



reaction 3

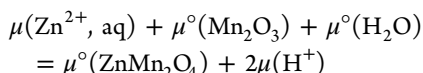


$$-16.18 \text{ eV} = -12.61 \text{ eV} - \text{pH} \times 0.476 \text{ eV} - 2\text{e}E_{\text{SHE}}$$

$$E_{\text{SHE}} = 1.78 \text{ V} - \text{pH} \times 0.237 \text{ V}$$

(13)

reaction 4

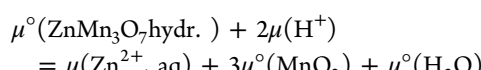


$$-13.17 \text{ eV} = -12.61 \text{ eV} - 0.118 \text{ eV} \times \text{pH}$$

$$\text{pH} = 4.75$$

(14)

reaction 6

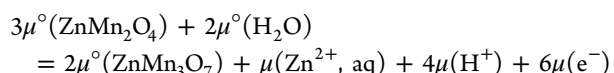


$$-17.83 \text{ eV} - \delta\mu - 0.118 \text{ eV} \times \text{pH} = -18.46 \text{ eV}$$

$$\text{pH} = 5.32 - \frac{\delta\mu(\text{eV})}{0.118}$$

(15)

reaction 7

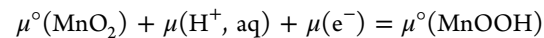


$$\begin{aligned} -42.75 \text{ eV} = -37.16 \text{ eV} - 2\delta\mu - 0.237 \text{ eV} \times \text{pH} \\ - 6\text{e}E_{\text{SHE}} \end{aligned}$$

$$E_{\text{SHE}} = 0.93 - \delta\mu/3\text{e} - \text{pH} \times 0.0395 \text{ V}$$

(16)

reaction 9

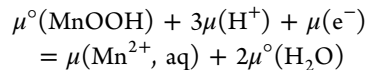


$$-4.83 \text{ eV} - \text{pH} \times 0.0592 \text{ eV} - \text{e}E_{\text{SHE}} = -5.81 \text{ eV}$$

$$E_{\text{SHE}} = 0.98 - \text{pH} \times 0.0592 \text{ V}$$

(17)

reaction 10



$$-5.81 \text{ eV} - \text{pH} \times 0.178 \text{ eV} - \text{e}E_{\text{SHE}} = -7.33 \text{ eV}$$

$$E_{\text{SHE}} = 1.52 - \text{pH} \times 0.178 \text{ V.}$$

(18)

AUTHOR INFORMATION

Corresponding Authors

Oleg Rubel – Department of Materials Science and Engineering, McMaster University, Hamilton, Ontario L8S 4L8, Canada; orcid.org/0000-0001-5104-5602; Email: rubelo@mcmaster.ca

Brian D. Adams – Salient Energy Inc., Dartmouth, Nova Scotia B3B 1C4, Canada; Email: brian@salientenergy.ca

Douglas G. Ivey – Department of Chemical and Materials Engineering, University of Alberta, Edmonton, Alberta T6G 1H9, Canada; Email: divey@ualberta.ca

Drew Higgins – Department of Chemical Engineering, McMaster University, Hamilton, Ontario L8S 4L8, Canada;

 orcid.org/0000-0002-0585-2670; Email: higgid2@mcmaster.ca

Authors

Thuy Nguyen Thanh Tran – Department of Chemical and Materials Engineering, University of Alberta, Edmonton, Alberta T6G 1H9, Canada; Salient Energy Inc., Dartmouth, Nova Scotia B3B 1C4, Canada

Storm Gourley – Department of Chemical Engineering, McMaster University, Hamilton, Ontario L8S 4L8, Canada

Sriram Anand – Department of Materials Science and Engineering, McMaster University, Hamilton, Ontario L8S 4L8, Canada; Department of Metallurgical and Materials Engineering, National Institute of Technology, Tiruchirappalli, Tamil Nadu 620015, India;  orcid.org/0000-0003-4703-4913

Andrew Van Bommel – Salient Energy Inc., Dartmouth, Nova Scotia B3B 1C4, Canada

Complete contact information is available at:
<https://pubs.acs.org/10.1021/acs.jpcc.2c01900>

Notes

The authors declare no competing financial interest.

ACKNOWLEDGMENTS

This work was supported by the Salient Energy, the NSERC Alliance program, the Mitacs Globalink program, the International Manganese Institute (IMnI) and a grant through the Mitacs Accelerate program (FR49801).

REFERENCES

- (1) Blanc, L. E.; Kundu, D.; Nazar, L. F. Scientific challenges for the implementation of Zn-ion batteries. *Joule* **2020**, *4*, 771–799.
- (2) Shoji, T.; Hishinuma, M.; Yamamoto, T. Zinc-manganese dioxide galvanic cell using zinc sulphate as electrolyte. Rechargeability of the cell. *J. Appl. Electrochem.* **1988**, *18*, 521–526.
- (3) Xu, C.; Li, B.; Du, H.; Kang, F. Energetic zinc ion chemistry: The rechargeable zinc ion battery. *Angew. Chem. Int. Ed.* **2012**, *51*, 933–935.
- (4) Sun, W.; Wang, F.; Hou, S.; Yang, C.; Fan, X.; Ma, Z.; Gao, T.; Han, F.; Hu, R.; Zhu, M.; et al. Zn/MnO₂ battery chemistry with H⁺ and Zn²⁺ coininsertion. *J. Am. Chem. Soc.* **2017**, *139*, 9775–9778.
- (5) Zhao, Q.; Chen, X.; Wang, Z.; Yang, L.; Qin, R.; Yang, J.; Song, Y.; Ding, S.; Weng, M.; Huang, W.; et al. Unravelling H⁺/Zn²⁺ synergistic intercalation in a novel phase of manganese oxide for high-performance aqueous rechargeable battery. *Small* **2019**, *15*, 1904545.
- (6) Li, Y.; Wang, S.; Salvador, J. R.; Wu, J.; Liu, B.; Yang, W.; Yang, J.; Zhang, W.; Liu, J.; Yang, J. Reaction mechanisms for long-life rechargeable Zn/MnO₂ batteries. *Chem. Mater.* **2019**, *31*, 2036–2047.
- (7) Chamoun, M.; Brant, W. R.; Tai, C.-W.; Karlsson, G.; Noréus, D. Rechargeability of aqueous sulfate Zn/MnO₂ batteries enhanced by accessible Mn²⁺ ions. *Energy Stor. Mater.* **2018**, *15*, 351–360.
- (8) Lee, B.; Yoon, C. S.; Lee, H. R.; Chung, K. Y.; Cho, B. W.; Oh, S. H. Electrochemically-induced reversible transition from the tunneled to layered polymorphs of manganese dioxide. *Sci. Rep.* **2015**, *4*, 6066.
- (9) Pan, H.; Shao, Y.; Yan, P.; Cheng, Y.; Han, K. S.; Nie, Z.; Wang, C.; Yang, J.; Li, X.; Bhattacharya, P.; et al. Reversible aqueous zinc/manganese oxide energy storage from conversion reactions. *Nat. Energy* **2016**, *1*, 16039.
- (10) Alfaruqi, M. H.; Islam, S.; Putro, D. Y.; Mathew, V.; Kim, S.; Jo, J.; Kim, S.; Sun, Y.-K.; Kim, K.; Kim, J. Structural transformation and electrochemical study of layered MnO₂ in rechargeable aqueous zincion battery. *Electrochimica Acta* **2018**, *276*, 1–11.
- (11) Chao, D.; Zhou, W.; Ye, C.; Zhang, Q.; Chen, Y.; Gu, L.; Davey, K.; Qiao, S.-Z. An electrolytic Zn-MnO₂ battery for high-voltage and scalable energy storage. *Angew. Chem. Int. Ed.* **2019**, *58*, 7823–7828.
- (12) Tran, T. N. T.; Jin, S.; Cuisinier, M.; Adams, B. D.; Ivey, D. G. Reaction mechanisms for electrolytic manganese dioxide in rechargeable aqueous zinc-ion batteries. *Sci. Rep.* **2021**, *11*, 20777.
- (13) Bischoff, C. F.; Fitz, O. S.; Burns, J.; Bauer, M.; Gentischer, H.; Birke, K. P.; Henning, H.-M.; Biro, D. Revealing the local pH value changes of acidic aqueous zinc ion batteries with a manganese dioxide electrode during cycling. *J. Electrochem. Soc.* **2020**, *167*, 020545.
- (14) Huang, Y.; Mou, J.; Liu, W.; Wang, X.; Dong, L.; Kang, F.; Xu, C. Novel insights into energy storage mechanism of aqueous rechargeable Zn/MnO₂ batteries with participation of Mn²⁺. *Nano-Micro Letters* **2019**, *11*, 49.
- (15) Jain, A.; Hautier, G.; Ong, S. P.; Moore, C. J.; Fischer, C. C.; Persson, K. A.; Ceder, G. Formation enthalpies by mixing GGA and GGA + U calculations. *Phys. Rev. B* **2011**, *84*, 045115.
- (16) Persson, K. A.; Waldwick, B.; Lazic, P.; Ceder, G. Prediction of solid-aqueous equilibria: Scheme to combine first-principles calculations of solids with experimental aqueous states. *Phys. Rev. B* **2012**, *85*, 235438.
- (17) Zeng, Z.; Chan, M. K. Y.; Zhao, Z.-J.; Kubal, J.; Fan, D.; Greeley, J. Towards first principles-based prediction of highly accurate electrochemical Pourbaix diagrams. *J. Phys. Chem. C* **2015**, *119*, 18177–18187.
- (18) Wang, Z.; Guo, X.; Montoya, J.; Nørskov, J. K. Predicting aqueous stability of solid with computed Pourbaix diagram using SCAN functional. *npj Comput. Mater.* **2020**, *6*, 160.
- (19) Pourbaix, M. *Atlas of electrochemical equilibria in aqueous solutions*, 2nd ed.; National Association of Corrosion Engineers: 1974.
- (20) Jacob, K. T.; Kumar, A.; Rajitha, G.; Waseda, Y. Thermodynamic data for Mn₃O₄, Mn₂O₃ and MnO₂. *High Temp. Mater. Processes (London)* **2011**, *30*, 459–472.
- (21) Bratsch, S. G. Standard electrode potentials and temperature coefficients in water at 298.15 K. *J. Phys. Chem. Ref. Data* **1989**, *18*, 1–21.
- (22) Maier, C. G.; Parks, G. S.; Anderson, C. T. The free energy of formation of zinc oxide. *J. Am. Chem. Soc.* **1926**, *48*, 2564–2576.
- (23) Hem, J. D.; Roberson, C. E.; Lind, C. J. Synthesis and stability of hetaerolite, ZnMn₂O₄, at 25°C. *Geochim. Cosmochim. Acta* **1987**, *51*, 1539–1547.
- (24) Hohenberg, P.; Kohn, W. Inhomogeneous electron gas. *Phys. Rev.* **1964**, *136*, B864–B871.
- (25) Kohn, W.; Sham, L. J. Self-consistent equations including exchange and correlation effects. *Phys. Rev.* **1965**, *140*, A1133–A1138.
- (26) Kresse, G.; Furthmüller, J. Efficient iterative schemes for ab initio total-energy calculations using a plane-wave basis set. *Phys. Rev. B* **1996**, *54*, 11169–11186.
- (27) Kresse, G.; Joubert, D. From ultrasoft pseudopotentials to the projector augmented-wave method. *Phys. Rev. B* **1999**, *59*, 1758–1775.
- (28) Blöchl, P. E. Projector augmented-wave method. *Phys. Rev. B* **1994**, *50*, 17953–17979.
- (29) Perdew, J. P.; Burke, K.; Ernzerhof, M. Generalized gradient approximation made simple. *Phys. Rev. Lett.* **1996**, *77*, 3865–3868.
- (30) Grimme, S.; Antony, J.; Ehrlich, S.; Krieg, H. A consistent and accurate ab initio parametrization of density functional dispersion correction (DFT-D) for the 94 elements H-Pu. *J. Chem. Phys.* **2010**, *132*, 154104.
- (31) Monkhorst, H. J.; Pack, J. D. Special points for Brillouin-zone integrations. *Phys. Rev. B* **1976**, *13*, 5188–5192.
- (32) Pan, H.; Ellis, J. F.; Li, X.; Nie, Z.; Chang, H. J.; Reed, D. Electrolyte effect on the electrochemical performance of mild aqueous zinc-electrolytic manganese dioxide batteries. *ACS Appl. Mater. Interfaces* **2019**, *11*, 37524–37530.
- (33) Poosapatip, A.; Vadnala, S.; Negrete, K.; Lan, Y.; Hutchison, J.; Zupan, M.; Madan, D. Rechargeable zinc-electrolytic manganese dioxide (EMD) battery with a flexible chitosan-alkaline electrolyte. *ACS Appl. Energy Mater.* **2021**, *4*, 4248–4258.

- (34) Biswal, A.; Tripathy, B. C.; Sanjay, K.; Subbaiah, T.; Minakshi, M. Electrolytic manganese dioxide (EMD): a perspective on worldwide production, reserves and its role in electrochemistry. *RSC Adv.* **2015**, *5*, 58255–58283.
- (35) Adams, B. D.; Ahn, J. H.; Brown, R. D.; Clarke, R. D.; Cuisinier, M.; Lee, J. P. S. Secondary electrochemical cell having a zinc metal negative electrode and mild aqueous electrolyte and methods thereof. 2019; patent WO/2019/095075.
- (36) Canepa, P.; Gautam, G. S.; Hannah, D. C.; Malik, R.; Liu, M.; Gallagher, K. G.; Persson, K. A.; Ceder, G. Odyssey of multivalent cathode materials: Open questions and future challenges. *Chem. Rev.* **2017**, *117*, 4287–4341.
- (37) Brady, J.; Humiston, G. E. *General chemistry, principles and structure*; John Wiley & Sons: New York, 1982.
- (38) Alfaruqi, M. H.; Gim, J.; Kim, S.; Song, J.; Jo, J.; Kim, S.; Mathew, V.; Kim, J. Enhanced reversible divalent zinc storage in a structurally stable α -MnO₂ nanorod electrode. *J. Power Sources* **2015**, *288*, 320–327.
- (39) Kitchaev, D. A.; Peng, H.; Liu, Y.; Sun, J.; Perdew, J. P.; Ceder, G. Energetics of MnO₂ polymorphs in density functional theory. *Phys. Rev. B* **2016**, *93*, 045132.
- (40) Aydinol, M. K.; Kohan, A. F.; Ceder, G.; Cho, K.; Joannopoulos, J. Ab initio study of lithium intercalation in metal oxides and metal dichalcogenides. *Phys. Rev. B* **1997**, *56*, 1354–1365.
- (41) Post, J. E.; Appleman, D. E. Chalcophanite, ZnMn₃O₇·3H₂O; new crystal-structure determinations. *Am. Mineral.* **1988**, *73*, 1401–1404.
- (42) Chevrier, V. L.; Ong, S. P.; Armiento, R.; Chan, M. K. Y.; Ceder, G. Hybrid density functional calculations of redox potentials and formation energies of transition metal compounds. *Phys. Rev. B* **2010**, *82*, 075122.
- (43) Wen, S.; Lee, J.-W.; Yeo, I.-H.; Park, J.; il Mho, S. The role of cations of the electrolyte for the pseudocapacitive behavior of metal oxide electrodes, MnO₂ and RuO₂. *Electrochim. Acta* **2004**, *50*, 849–855.
- (44) Oberholzer, P.; Tervoort, E.; Bouzid, A.; Pasquarello, A.; Kundu, D. Oxide versus nonoxide cathode materials for aqueous Zn batteries: An insight into the charge storage mechanism and consequences thereof. *ACS Appl. Mater. Interfaces* **2019**, *11*, 674–682.
- (45) Magar, B. A.; Paudel, N.; Lambert, T. N.; Vasiliev, I. Ab initio studies of discharge mechanism of MnO₂ in deep-cycled rechargeable Zn/MnO₂ batteries. *J. Electrochem. Soc.* **2020**, *167*, 020557.
- (46) Guo, X.; Li, J.; Jin, X.; Han, Y.; Lin, Y.; Lei, Z.; Wang, S.; Qin, L.; Jiao, S.; Cao, R. A hollow-structured manganese oxide cathode for stable Zn-MnO₂ batteries. *Nanomaterials* **2018**, *8*, 301.
- (47) Huang, J.; Wang, Z.; Hou, M.; Dong, X.; Liu, Y.; Wang, Y.; Xia, Y. Polyaniline-intercalated manganese dioxide nanolayers as a high-performance cathode material for an aqueous zinc-ion battery. *Nat. Commun.* **2018**, *9*, 2906.
- (48) Khamsanga, S.; Pornprasertsuk, R.; Yonezawa, T.; Mohamad, A. A.; Kheawhom, S. δ -MnO₂ nanoflower/graphite cathode for rechargeable aqueous zinc ion batteries. *Sci. Rep.* **2019**, *9*, 8441.
- (49) Han, M.; Huang, J.; Liang, S.; Shan, L.; Xie, X.; Yi, Z.; Wang, Y.; Guo, S.; Zhou, J. Oxygen defects in β -MnO₂ enabling high-performance rechargeable aqueous zinc/manganese dioxide battery. *iScience* **2020**, *23*, 100797.
- (50) Chen, L.; Yang, Z.; Cui, F.; Meng, J.; Jiang, Y.; Long, J.; Zeng, X. Ultrathin MnO₂ nanoflakes grown on N-doped hollow carbon spheres for high-performance aqueous zinc ion batteries. *Mater. Chem. Front.* **2020**, *4*, 213–221.
- (51) Zhou, W.; Wang, A.; Huang, A.; Chen, M.; Tian, Q.; Chen, J.; Xu, X. Hybridizing δ -type MnO₂ with lignin-derived porous carbon as a stable cathode material for aqueous Zn-MnO₂ batteries. *Front. Energy Res.* **2020**, *8*, 182.
- (52) Zeng, L.; Zhang, G.; Huang, X.; Wang, H.; Zhou, T.; Xie, H. Tuning crystal structure of MnO₂ during different hydrothermal synthesis temperature and its electrochemical performance as cathode material for zinc ion battery. *Vacuum* **2021**, *192*, 110398.
- (53) Moon, H.; Ha, K.-H.; Park, Y.; Lee, J.; Kwon, M.-S.; Lim, J.; Lee, M.-H.; Kim, D.-H.; Choi, J. H.; Choi, J.-H.; et al. Direct proof of the reversible dissolution/deposition of Mn²⁺/Mn⁴⁺ for mild-acid Zn-MnO₂ batteries with porous carbon interlayers. *Adv. Sci.* **2021**, *8*, 2003714.
- (54) Lee, B.; Seo, H. R.; Lee, H. R.; Yoon, C. S.; Kim, J. H.; Chung, K. Y.; Cho, B. W.; Oh, S. H. Critical role of pH evolution of electrolyte in the reaction mechanism for rechargeable zinc batteries. *ChemSusChem* **2016**, *9*, 2948–2956.

CAS BIOFINDER DISCOVERY PLATFORM™

ELIMINATE DATA SILOS. FIND WHAT YOU NEED, WHEN YOU NEED IT.

A single platform for relevant, high-quality biological and toxicology research

Streamline your R&D

CAS A division of the American Chemical Society